

Superpixel-based Efficient Sampling for Learning Neural Fields from Large Input

Anonymous Authors

ABSTRACT

In recent years, novel view synthesis methods using neural implicit fields have gained popularity due to their exceptional rendering quality and rapid training speed. However, the computational cost of volumetric rendering has increased significantly with the advancement of camera technology and the consequent rise in average camera resolution. Despite extensive efforts to accelerate the training process, the training duration remains unacceptable for high-resolution inputs. Therefore, the development of efficient sampling methods is crucial for optimizing the learning process of neural fields from a large volume of inputs. In this paper, we introduce a novel method named Superpixel Efficient Sampling (SES), aimed at enhancing the learning efficiency of neural implicit fields. Our approach optimizes pixel-level ray sampling by segmenting the error map into multiple superpixels using the SLIC algorithm, and dynamically updating their errors during training to increase ray sampling in areas with higher rendering errors. Compared to other methods, our approach leverages the flexibility of superpixels, effectively reducing redundant sampling while considering local information. Our method not only accelerates the learning process but also improves the rendering quality obtained from a vast array of inputs. We conduct extensive experiments to evaluate the effectiveness of our method across several baselines and datasets. The code will be released.

KEYWORDS

Neural Radiance Fields, Novel view synthesis, Large Input

1 INTRODUCTION

Novel view synthesis(NVS) has always been a hot research topic in computer vision, with wide-ranging applications in virtual reality, medical imaging, and augmented reality. In recent years, NVS methods that represent scenes using neural fields have gradually become prevailing due to their promising results [16–18, 21, 24, 41, 42, 46]. These methods represent the scenes with Deep Neural Networks (DNNs) and render the scenes through volume rendering. Compared with traditional Multi-View Stereo (MVS) methods [3, 5, 9, 11, 12, 40], they can easily handle textureless surfaces and interpolate unseen areas via regularization techniques [13]. However, the volume rendering of huge sampled points brings substantial

Permission to make digital or hard copies of all or part of this work for personal or
Unpublished working draft. Not for distribution. contributed
for profit or commercial advantage and that copies bear this notice and the full citation
on the first page. Copyrights for components of this work owned by others than the
author(s) must be honored. Abstracting with credit is permitted. To copy otherwise, or
republish, to post on servers or to redistribute to lists, requires prior specific permission
and/or a fee. Request permissions from permissions@acm.org.

ACM MM, 2024, Melbourne, Australia

© 2024 Copyright held by the owner/author(s). Publication rights licensed to ACM.

ACM ISBN 978-x-xxxx-xxxx-x/YY/MM

<https://doi.org/10.1145/nnnnnnn.nnnnnnn>

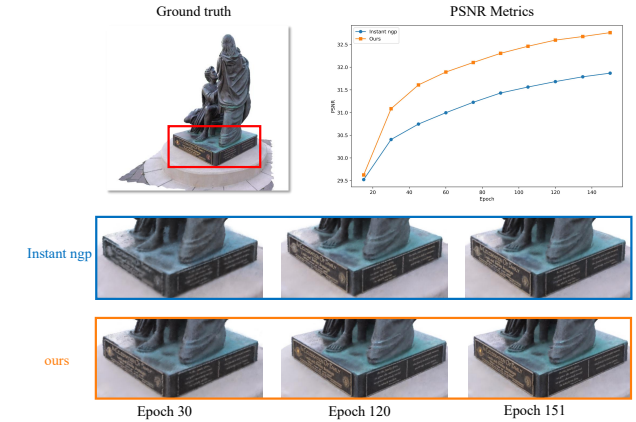


Figure 1: Comparison between Instant NGP and Our Method: The top right corner displays PSNR curves for both methods on the test set, while the visualization below showcases their rendering results. Incorporating our method enhances the convergence speed and rendering quality of Instant NGP noticeably.

computational overhead, which becomes even more severe with increasing image resolution.

For novel view synthesis, the resolution of input images directly determines the upper limit of reconstruction quality. With the advancement of camera technology, the resolution of captured images continues to increase. However, high-resolution images not only capture more details but also bring a substantial amount of redundant data. Therefore, traditional random pixel sampling methods [20, 34] become overwhelmed by the huge number of pixels in high-resolution inputs. [44] employs a patch sampling strategy combined with an encoder-decoder structure. They use the encoder to encode 3D geometric information and the decoder to render high-resolution outputs. [35] introduces color-guided ray sampling. They guide the sampling of rays by color and depth, allowing the rays to pass through regions with richer spatial information. However, their method does not simultaneously consider both color and rendering errors, and the redundant sampling of rays results in slower convergence on high-resolution images.

To address the challenge of large input, we introduce a Superpixel-based Efficient Sampling (SES) method for learning neural fields. Our core idea is to increase the number of light paths to acquire more information, especially in regions with significant rendering errors, thereby reducing redundancy in sampling. Simultaneously, we aim to optimize the sampling of light rays to consider local image information. We first employ the SLIC algorithm to segment the input image into different superpixels, where each superpixel represents distinct local information. Compared to other segmentation

117 methods like quadtree, superpixels can significantly reduce redundancy.
 118 In subsequent steps, we treat superpixels as the smallest
 119 processing unit. We set different sampling probabilities for different
 120 superpixels based on their rendering errors, continuously update
 121 them during training, and incorporate the rendering errors into
 122 the loss function. We apply our method to several popular NeRF
 123 algorithms and test it on multiple common datasets. Our image
 124 rendering quality reached the state of the art at different resolutions,
 125 and integrating our method did not incur additional computational
 126 overhead. In summary, our main contributions can be summarized
 127 as follows:

- We propose an efficient and effective sampling method for learning neural fields from large input. By segmenting the image into superpixels, we reduce light ray redundancy, improve sampling efficiency, and take into account local sampling information.
- We have devised a new loss function to expedite the convergence of the network in regions with significant rendering errors.
- We conduct comprehensive experiments based on popular neural field methods across several datasets, demonstrating the advantages of the proposed method.

2 RELATED WORK

2.1 Novel view Synthesis

In graphics research, the pursuit of Novel View Synthesis (NVS) hinges on adeptly handling intermediate 3D scene representations. Previous endeavors have focused on exploring suitable 3D representations: Mesh-based or pointcloud-based methods[2, 4, 6, 27, 39] often rely on depth information or structure from motion(SFM)[28] techniques for geometric shape restoration, presenting challenges in rendering realistic images. While approaches utilizing multi-plane images(MPIs)[7, 19, 32, 33, 38, 51] to express scenes as feature maps or stacked images can yield high-quality renderings, they constrain the variability of perspectives. Voxel-based representations[14, 17, 25, 29, 30, 36] offer swift image rendering but face limitations in resolution. By modeling scenes as neural implicit fields[20, 22, 31, 47], greater flexibility is attained alongside high-quality image generation: Differentiable Volume Rendering (DVR)[23] and Implicitly Differentiable Renderers (IDR)[48] have demonstrated promising results, albeit still requiring precise object mask inputs during training. The year 2020 saw the groundbreaking introduction of NeRF[20], revolutionizing NVS through volume rendering. NeRF employs neural networks to model spatial 3D coordinates and view directions as volume density and color, employing alpha blending for pixel color rendering, resulting in remarkable outcomes. NeRF's advent has significantly advanced the domains of new view synthesis, 3D reconstruction, point cloud rendering, and beyond.

2.2 Training acceleration

NeRF employs volume rendering to render pixel colors, and to bring sampling points closer to the surface, it introduces a two-stage sampling method along the rays. However, such an approach typically demands 1-2 days or even several days for training completion. To expedite NeRF training, ENeRF[10] utilizes the geometric

175 features of the scene to guide surface sampling. Some methods
 176 leverage explicit modeling techniques to accelerate scene training:
 177 kilo NeRF[26] decomposes NeRF into multiple small MLPs for faster
 178 training, while DVGO[34], Plenoxels[8], and similar works employ
 179 learnable explicit meshes to expedite training. Instant ngp[21] utili-
 180 zes multi-resolution hash encoding with a hash table and jump
 181 sampling to swiftly approach the scene surface during training. The
 182 aforementioned works focus on accelerating sampling strategies in
 183 space; Wang et al.[50] use a quadtree to guide sampling, reducing
 184 the number of sampled rays to accelerate training, while Sun et
 185 al[35] efficiently sample rays by filtering them using images and
 186 depth information. These methods greatly accelerate NeRF train-
 187 ing, although they may encounter limitations when high-resolution
 188 images are input.

2.3 High-resolution Synthesis

To handle high-resolution image inputs and generate high-resolution
 191 images, 4k-NeRF[44] encodes high-resolution images into feature
 192 maps. After training, a decoder is used to decode these feature
 193 maps into high-resolution images. This method reduces the com-
 194 putational burden during NeRF training. However, joint training of
 195 the encoder-decoder with NeRF still requires a considerable amount
 196 of time. UHD-NeRF[15] reconstructs higher-resolution images by
 197 using a combination of neural networks and point cloud represen-
 198 tations. It intends to reconstruct the low-frequency components
 199 of the scene using MLP and the high-frequency components using
 200 point clouds. It is worth noting that both methods mentioned above
 201 use patch sampling to avoid excessive memory consumption. While
 202 patches can capture local information in the scene, their fixed shape
 203 may lead to fragmented image information.

3 METHOD

Our primary objective is to address the slow convergence and scattered sampling issues brought about by high-resolution inputs, ensuring superior rendering results within the same training time-frame. Firstly, in Section 3.1, we introduce the NeRF[20] and SLIC[1] segmentation algorithm, forming our work's foundation. Subsequently, in Section 3.2, we present our two-stage segmentation method and how we utilize superpixels to guide sampling. Finally, in Section 3.3, we demonstrate how our method integrates into existing baselines. Figure 2 illustrates our entire pipeline.

3.1 Preliminaries

NeRF: In NeRF[20], a 3D scene as a continuous function which takes as input 3D position $x = (x, y, z)$ and viewing direction $d = (\theta, \phi)$ and predicts the radiance color c and volume density σ . The architecture of f_θ is chosen such that only the color c depends on the viewing direction d . This allows the modeling of view-dependent effects like specularities and reflections while also encouraging a consistent geometry to be learned. In a deterministic pre-processing step x and d are transformed by a positional encoding γ which promotes learning of high-frequency details. NeRF is typically parametrized by a multilayer perceptron (MLP) $f : (\gamma(x), d) = (c, \sigma)$. To render a pixel by a given camera pose, the expected color $\hat{C}(r)$ of a camera ray $r = o + td$ through the pixel

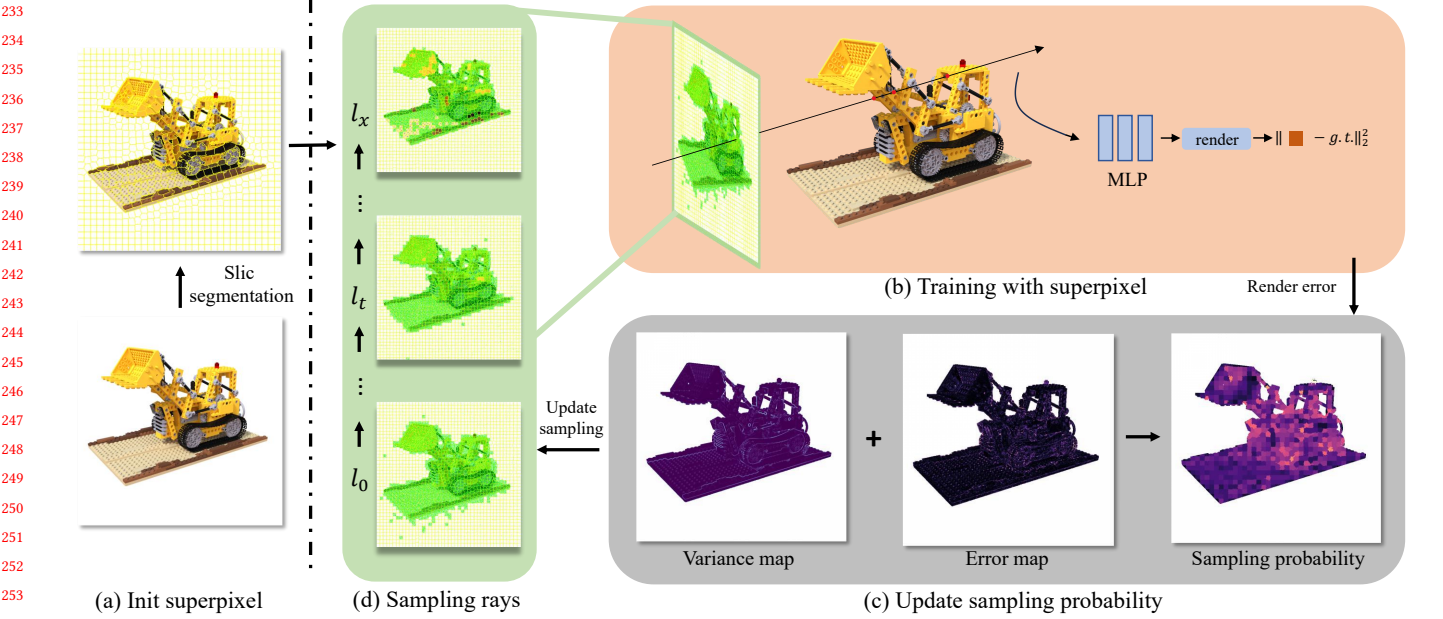


Figure 2: Overview of our pipeline. (a) Firstly, we initialize the segmentation of input images using the SLIC algorithm. After a period of training, secondary segmentation is conducted at certain locations, yielding the final superpixels, and generating sampled rays. (b) The sampled rays are trained and the rendering error is recorded after each session for subsequent updates. (c) After ray sampling training, the rendering error for each superpixel is computed based on accumulated data. A sampling probability map is generated by combining pixel variances, and sampled rays are regenerated accordingly.

that shots from the camera o in direction d can be calculated as

$$C(r) = \int_{t_n}^{t_f} T(t) \sigma(r(t)) c(r(t), d) dt \quad (1)$$

where

$$T(t) = \exp(-\int_{t_n}^{t_f} \sigma(r(t)) dt) \quad (2)$$

the accumulated transmittance indicates the probability that a ray travels from t_n to t without hitting any particle. NeRF is trained to minimize the mean-squared error(MSE) between the predicted renderings and the corresponding ground-truth color:

$$\mathcal{L}_{\text{MSE}} = \sum_{p \in \mathcal{P}} \|\hat{C}(r_p) - C(r_p)\|_2^2 \quad (3)$$

where \mathcal{P} denotes all pixels of training set images, $\hat{C}(r_p)$ and $C(r_p)$ are the ground truth and output color of p .

SLIC: Simple Linear Iterative Clustering(SLIC)[1] is a fast and effective algorithm for image segmentation. As shown in algorithm1 combines superpixel methods with K-means clustering to cluster pixels in the color space, thus achieving image segmentation. SLIC first grids pixels into compact superpixels and then groups these superpixels into segments based on pixel similarity and distance measurements. By controlling superpixels' compacity and distance parameters, SLIC can significantly reduce computational complexity while preserving image details. Furthermore, SLIC excels in preserving boundary information of the image, allowing the segmentation results better to retain the sharpness and continuity of

Algorithm 1 SLIC superpixel segmentation

```

1: /* Initialization */
2: Initialize cluster centers  $C_k = [l_k, a_k, b_k, x_k, y_k]^T$  by sampling
   pixels at regular grid steps  $S$ .
3: Move cluster centers to the lowest gradient position in a 33
   neighborhood.
4: Set label  $l(i) = -1$  for each pixel  $i$ .
5: Set distance  $d(i) = \infty$  for each pixel  $i$ .
6: repeat
7:   for each cluster center  $C_k$  do
8:     for pixel  $i$  in a  $2S * 2S$  region around  $C_k$  do
9:       Compute the distance  $D$  between  $C_k$  and  $i$ .
10:      if  $D < d(i)$  then
11:        set  $d(i) = D$ 
12:        set  $l(i) = k$ 
13:      endif
14:    endfor
15:  endfor
16:  /* Update */
17:  Compute new cluster centers.
18:  Compute residual error  $E$ .
19: until  $E \leq \text{threshold}$ 

```

object boundaries. The distance between C_k and i is calculated by

349 the following formula:

$$350 \quad D = \sqrt{(L - L_i)^2 + (a - a_i)^2 + (b - b_i)^2 + \left(\frac{S - S_i}{S_N}\right)^2} \quad (4)$$

351 where L, a, b are the values in the LAB color space of the pixel, S
 352 is the position of the pixel, L_i, a_i, b_i are the values in the LAB color
 353 space of the center of the superpixel block, S_i is the position of the
 354 center of the superpixel block, S_N is the normalization factor, equal
 355 to image size divided by the number of superpixel numbers.

356 3.2 Superpixel guide sampling

357 NeRF[20] perceives space by learning a color-constrained network
 358 to output color and density information of three-dimensional spatial
 359 points. Compared to simple regions in space, complex regions re-
 360 quire more iterations for the network to better learn spatial infor-
 361 mation. Previous methods[35, 50] have attempted multiple sampling in
 362 regions with large rendering errors or drastic color changes while
 363 reducing sampling in areas with small rendering errors to achieve
 364 better results. Redundant computations resulting from insufficient
 365 partitioning by quadtrees and other segmentation methods increase
 366 continuously with input scale and are not feasible. Methods guiding
 367 computation through color gradients also struggle with handling
 368 large-scale image blocks. To address these issues, we use the SLIC[?]
 369] algorithm to segment images into different superpixels, which
 370 serve as the smallest processing units for guiding sampling. Due to
 371 the characteristics of superpixels, the problem of insufficient parti-
 372 tioning caused by structures like quadtrees is resolved, reducing
 373 computational overhead in single processing instances.

374 **Image to superpixel** During the training process, we will up-
 375 date the SLIC segmentation results twice, which enables the segmen-
 376 tation to focus on rendering errors while conforming to geometric
 377 constraints. At the beginning of training, we will employ the SLIC
 378 algorithm to partition the input RGB image into superpixels.

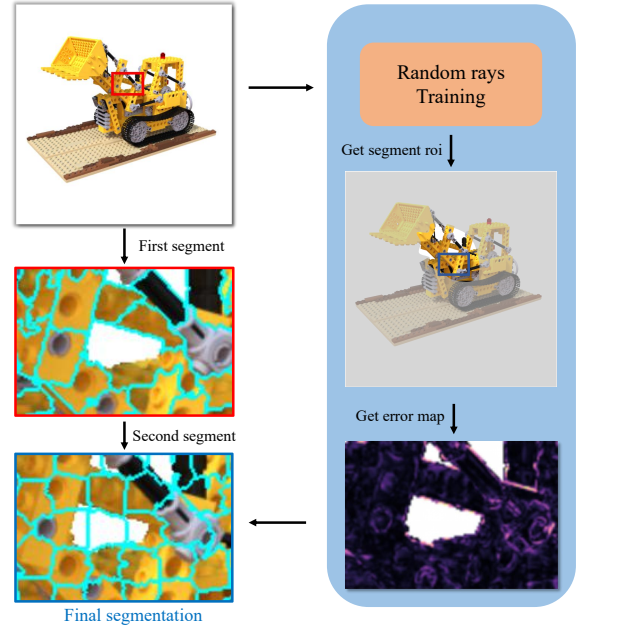
$$379 \quad \ell^i = F(T_{CIE}(Image)), \ell^i \in L \quad (5)$$

380 where ℓ^i represents the i th superpixel in the image, L denotes the
 381 collection of all superpixels segmented in the image, F represents
 382 the SLIC algorithm1, with its process outlined in Algorithm 1, and
 383 T signifies the transformation of the image from the RGB color
 384 space to the ICE color space.

385 Then, during the training process, we will update the superpixel
 386 segmentation results for the second time to make the segmentation
 387 more focused on areas with larger rendering errors. However, it is
 388 not necessary to update all superpixels to avoid disrupting the orig-
 389 inal segmentation structure. Refer to Figure 3, we will concentrate
 390 the re-segmentation effort on the areas with the largest rendering
 391 errors and their adjacent areas, using the masked slic algorithm
 392 to re-segment these regions. In the re-segmentation process, both
 393 RGB color and rendering error are considered simultaneously. First,
 394 the rendering error is mapped to the RGB color space, and then it
 395 is converted to the CIE color space. During the distance calculation
 396 with the SLIC algorithm, the distances in both the RGB and CIE
 397 color spaces are considered.

$$398 \quad C_k = \beta_0 T_{CIE}(I) + (1 - \beta_0) T_{CIE}(R) \quad (6)$$

399 Where I represents the portion of the input RGB image that needs
 400 to be re-segmented, R represents the portion of the render error



408
 409
 410
 411
 412
 413
 414
 415
 416
 417
 418
 419
 420
 421
 422
 423
 424
 425
 426
 427
 428
 429
 430
 431
 432
 433
 434
 435
 436
 437
 438
 439
 440
 441
 442
 443
 444
 445
 446
 447
 448
 449
 450
 451
 452
 453
 454
 455
 456
 457
 458
 459
 460
 461
 462
 463
 464

Figure 3: Two rounds of segmentation in our approach: firstly, an initial segmentation is performed on the RGB image. Following a training period, areas necessitating re-segmentation are identified, and re-segmentation is carried out by considering both rendering errors and RGB colors.

456 that needs to be recalculated. This portion is replicated three times
 457 to meet the dimensional requirements for the transformation to the
 458 ICE space. β_0 is a regularization term used to adjust the weights
 459 between the RGB image and the render error.

460 **Sample with superpixel** We employ superpixels to guide the
 461 pixel-level sampling during the training process. Initially, we com-
 462 pute the average sampling error within each superpixel. Each su-
 463 perpixel's error ℓ_{error}^i is computed as follows:

$$464 \quad \ell_{error}^i = \frac{1}{N} \sum_{j \in N} r_j \quad (7)$$

465 where N represents the number of pixels sampled in this segment,
 466 and r_j denotes the rendering error of the current pixel.

467 We will calculate the sampling probability for each superpixel
 468 based on its rendering error and RGB color. Initially, we will ex-
 469 clude superpixels with negligible errors, corresponding to either
 470 blank areas in the scene or well-learned regions. Rendering error
 471 serves as the primary indicator for sampling probability calculation.
 472 However, due to significant variations in rendering error scales
 473 within the scene, sampling tends to concentrate on a few super-
 474 pixels. To ensure comprehensive scene coverage, we employ the
 475 square root of the error as a representation of sampling probability.
 476 Despite the stochastic nature of sampling, sampling error may not
 477 fully capture sampling probability. Thus, we supplement this with
 478 RGB information. By computing the variance of colors within each
 479 superpixel, we collectively determine the sampling probability for
 480 each superpixel. Therefore, the sampling probability $g(\ell_{error}^i)$ for

each superpixel can be calculated as follows:

$$\ell_{error_p}^i = \begin{cases} \frac{clamp(t, \sqrt{\max(\ell_{error}^i)}), & \text{if } \ell_{error}^i > t \\ \sqrt{\max(\ell_{error}^i)}, & \text{if } \ell_{error}^i \leq t \\ 0, & \text{else} \end{cases} \quad (8)$$

$$\ell_{std_p}^i = \sqrt{\frac{1}{m} \sum_{x,y} [c(x,y) - \bar{c}]^2}, \quad x, y \in \ell^i. \quad (9)$$

$$\ell_p^i = \lambda_{error} \cdot \ell_{error_p}^i + \lambda_{std} \cdot \ell_{std_p}^i \quad (10)$$

where t denotes the minimum error threshold we set. We normalize the sampling probability of the rendering error component to lie between 0 and 1, m represents the number of pixels in the current superpixel, and \bar{c} denotes the average color within the superpixel. λ_{error} and λ_{std} are the coefficients for the sampling probabilities. We adjust these coefficients to balance the weights of the two probabilities.

3.3 Superpixel guide sampling

We integrate superpixel sampling into NeRF training and employ a series of strategies to adapt to high-resolution inputs, thereby enhancing the rendering quality of NeRF.

Training Progress. Our training process is illustrated in Figure 2. Initially, we employ a random sampling method for training while updating the errors of superpixels in each training iteration. After the secondary segmentation computation, we utilize superpixels to guide sampling and ray generation, concurrently accumulating rendering errors. Upon completion of training for all rays generated in a single sampling, we update the superpixel errors and regenerate rays.

Loss Design. We optimize the parameters of the MLP using pixel-level Mean Squared Error (MSE) loss \mathcal{L}_{mse} and superpixel loss \mathcal{L}_{sp} . Our total loss is computed as follows:

$$\mathcal{L} = \lambda_{mse} \cdot \mathcal{L}_{mse} + \lambda_{sp} \cdot \mathcal{L}_{sp} \quad (11)$$

The calculation method of \mathcal{L}_{sp} is as follows:

$$\mathcal{L}_{sp} = \ell_{error}^i + 0.001 \cdot \ell_{std_p}^i \quad (12)$$

Due to the strong bias of \mathcal{L}_{sp} , λ_{sp} is typically set to be three to four orders of magnitude smaller than the λ_{mse} during the training process.

Progressive Training. In NeRF[20] and its related works, position encoding is utilized to enable MLPs to learn more high-frequency information. However, in practical tests, we found that while higher frequency position encoding captures more detailed information, it leads to slower convergence. In our work, we focus on enabling the training to rapidly learn the scene's low-frequency information in the initial, low-frequency stages. Therefore, we adopt a strategy similar to that used in NeuS2[42] and FreeNerf[45], gradually increasing the bandwidth of the position encoding during the training process. In NeRF, the representation of position encoding is as follows.

$$\gamma_L(\mathbf{x}) = [\sin(\mathbf{x}), \cos(\mathbf{x}), \dots, \sin(2^{L-1}\mathbf{x}), \cos(2^{L-1}\mathbf{x})] \quad (13)$$

$$\gamma'_L(\mathbf{x}) = \gamma_L(\mathbf{x}) * M(i) \quad (14)$$

where, L represents the maximum frequency in position encoding, and $\gamma_L(\mathbf{x})$ defines the specific formulation of position encoding.

The position encoding used in our work is $\gamma'_L(\mathbf{x})$ which is formed by multiplying $\gamma_L(\mathbf{x})$ with M which is a mask with the same dimension as $\gamma'_L(\mathbf{x})$, designed to mask the high-frequency components, with its specific parameters controlled by the number of input iterations i . In practical training, we set the maximum frequency of the position encoding to a quarter of its original value, which is gradually increased as the training progresses and the resolution enhances.

4 EXPERIMENTS

4.1 Implementation Details

In comparison to structures like quad-trees, superpixels do not possess similar tree-like structures to minimize sampling redundancy. To fully leverage hardware performance, we provide our method's implementation on CUDA. In our implementation, for synthetic datasets, we set β_0 to 0.8 as per Equation 6, λ_{mse} as 1, λ_{sp} as 1e-6, whereas for real datasets, we choose β_0 as 0.65, λ_{mse} as 1, λ_{sp} as 1e-8. Our method can be seamlessly integrated into the popular NeRF framework. To demonstrate the efficiency of our approach, we selected Instant-NGP[21] and DVGO[34] as our baselines, both known for their fast training speeds within the NeRF domain. It is worth noting that, in our experiments, we utilized an open-source implementation of Instant NGP, namely the nerf-template, which is a clean version derived from the open-source project torch-ngp[37]. We employed this implementation in our experiments as a replacement for the original Instant NGP. We conducted experiments using a single NVIDIA RTX 4090 GPU.

4.2 Dataset

We tested our method on the currently popular NeRF dataset to demonstrate its superiority. We conducted experiments on three datasets: eight synthetic 360° scenes provided by NeRF, four scenes from Tank and Template, and eight real scenes from MipNerf 360 dataset. We also provided ablation experiments to validate our method. We evaluate the quality of view synthesis for ground truth from the same pose using three metrics: PSNR, SSIM[43], and LPIPS[49].

4.3 Realistic Synthetic 360 evaluation

The Realistic Synthetic 360 evaluation dataset[20] is a commonly used benchmark in the NeRF field. Using Blender, it renders eight scenes, each with distinct characteristics, and generates 100 training images per scene, making it a popular choice for multi-view reconstruction benchmarks. While the native renderings are at a resolution of 800x800, based on the provided Blender files, we generated images at higher resolution(1600x1600, 3200x3200). These newly rendered high-resolution images maintain the original viewing angles but offer enhanced clarity. Due to memory constraints, we conducted experiments only at resolutions of 800 and 1600 on DVGO.

The quantitative results of our method are presented in Table 1. We compare our approach with the baseline at different scales, revealing superior performance across all resolutions, notably in Hotdog and Lego scenes. Visualizations of our results are illustrated in Figure 4, demonstrating enhanced scene details and reduced

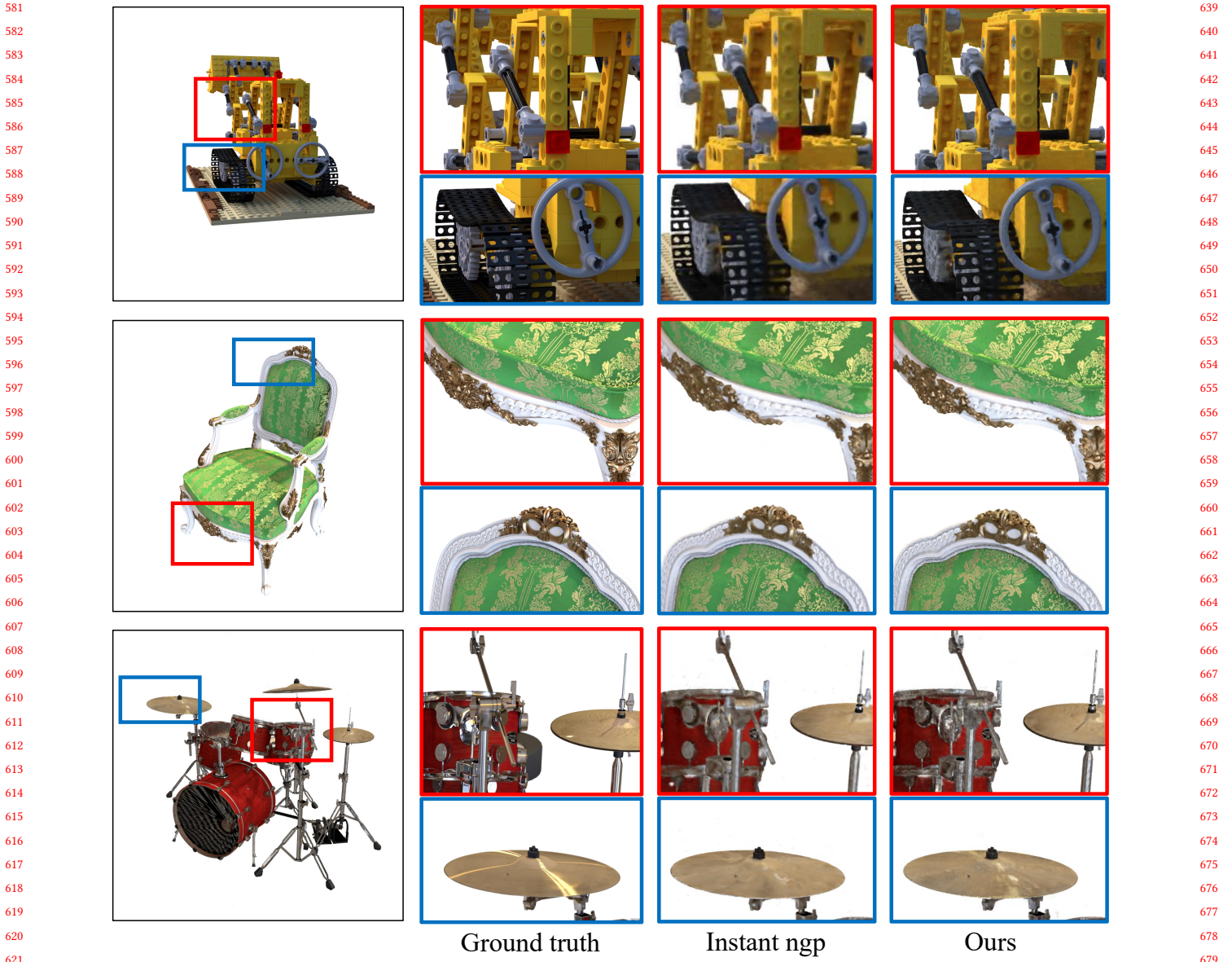


Figure 4: Results of NeRF Synthetic 3200x3200. The figure showcases the results of our method combined with Instant NGP on high-resolution inputs from the NeRF synthetic dataset. With the incorporation of our method, the rendered images exhibit increased detail and high-frequency information.

artifacts, particularly evident in scenarios with large-scale inputs, upon integration of our method.

4.4 MipNeRF 360

MipNeRF 360 is a commonly used real-world unbounded scene dataset, comprising intricate scenes without boundaries. We conducted experiments on seven distinct scenes within this dataset. Each scene dataset includes original 4K images alongside their corresponding downsampled versions. We evaluated the 2x and 4x downsampled input images. Results demonstrate that our proposed

approach outperforms baseline models, particularly excelling in high-resolution scenes.

In Table 2, we present the quantitative results of our experiments, demonstrating that our method adapts well to both resolutions and consistently improves performance over the selected baselines. Our visual results are showcased in Figure 5, where it can be observed that our method reconstructs more details compared to the baselines, particularly evident with high-resolution inputs. We also monitored the impact of incorporating our method on the training time of the baseline. The addition of our method results in only a

Method	Blender 800x800			Blender 1600x1600			Blender 3200x3200		
	PSNR↑	SSIM↑	LPIPS↓	PSNR↑	SSIM↑	LPIPS↓	PSNR↑	SSIM↑	LPIPS↓
DVGO	31.77	0.955	0.055	30.30	0.942	0.087	-	-	-
DVGO(ours)	31.88	0.955	0.057	30.57	0.951	0.086	-	-	-
DVGO(wo mask)	31.15	0.951	0.062	30.06	0.940	0.090	-	-	-
instant ngp	30.68	0.945	0.078	29.79	0.935	0.108	28.72	0.942	0.084
instant ngp(ours)	31.11	0.948	0.078	30.99	0.942	0.088	29.28	0.944	0.080

Table 1: These are the quantitative results for the NeRF synthetic dataset. As demonstrated, our method shows performance improvements in the majority of the scenes.

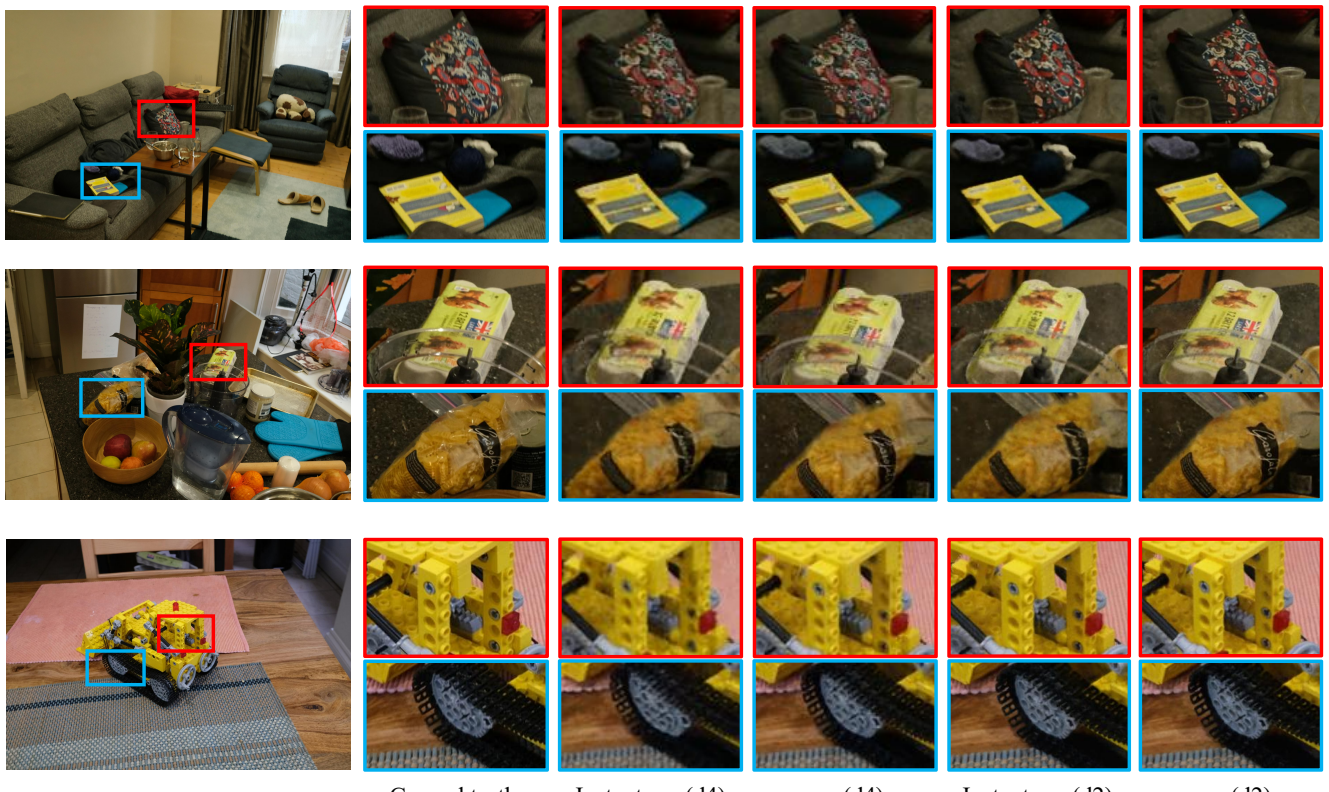


Figure 5: The experimental results graph for MipNeRF. We compared our visualization results with Instant NGP at two downsampling rates: 2x and 4x. Our method consistently produces higher-quality images at both resolutions, with a more pronounced effect at higher resolutions."

slight increase in training time, posing no significant computational burden.

4.5 TanksAndTemple

The Tankandtemple dataset provides eight scenes at a resolution of 1080p. We tested our method on four bounded scenes within the dataset. As shown in Table 3, our method achieves state-of-the-art performance in several scenes provided by the dataset. Figure1 in the paper demonstrates the convergence speed and final rendering results of our method compared to the baseline. We observe faster

convergence and better image quality with our method. Figure 6 illustrates the rendering results of our method at the edges, where we capture high-frequency information more effectively, resulting in clearer rendered images.

4.6 Ablation studies

Our method employs a two-stage segmentation approach, aiming to balance the influence of color and error on segmentation. To validate the effectiveness of our method, we separately test the results of segmentation based solely on RGB color and solely on

Method	(b) Mip NeRF 360.				Times↓	Mip NeRF down 2			
	PSNR↑	Mip NeRF down 4 SSIM↑	LPIPS↓	PSNR↑		SSIM↑	LPIPS↓	Times↓	
DVGO	25.65	0.705	0.381	626		25.15	0.668	0.463	654
DVGO(ours)	26.11	0.731	0.372	641		25.62	0.671	0.442	701
instant ngp	25.27	0.702	0.376	274		24.83	0.613	0.482	290
instant ngp(ours)	27.37	0.733	0.361	281		25.81	0.634	0.462	299

Table 2: These are the quantitative results for the MipNeRF dataset. As demonstrated, our method shows performance improvements in the majority of the scenes.

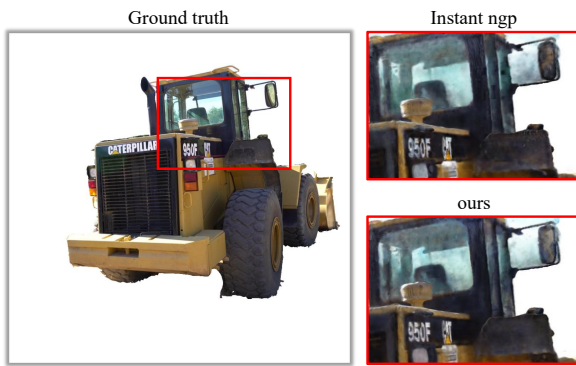


Figure 6: We compare the reconstruction results of our method and the baseline at the edges, where our method provides clearer edge information.

Method	Barn	Caterpillar	Family	Truck	Mean
dvg	26.87	25.70	33.73	27.08	28.35
dvg(ours)	27.01	25.92	33.77	27.69	28.60
torch ngp	26.18	25.04	31.87	26.67	27.44
torch ngp(ours)	26.39	25.35	32.76	26.82	27.83

Table 3: These are the quantitative results for the TankandTtemplate dataset. As demonstrated, our method shows performance improvements in the majority of the scenes.

rendering error. We use Instant NGP as the baseline and test on the NeRF synthetic dataset. As shown in the table 4, segmentation based solely on RGB color leads to unstable results. While it achieves good performance in some scenes, the results in certain scenes become unacceptable. On the other hand, using error-based segmentation alone results in relatively stable improvements, but areas with large errors may overlook structural information in the scene. Therefore, our two-stage sampling strategy strikes a good balance between stability and rendering quality.

5 CONCLUSION

In this paper, we introduce a method called SPS which employs superpixels to guide the pixel-level ray sampling process during NeRF training, allowing for the processing of large-scale image inputs

Method	chair	drums	ficus	hotdog	lego
instant ngp	29.06	24.86	29.87	33.98	30.40
instant ngp(rgb)	27.53	26.10	28.92	34.01	32.13
instant ngp(error)	29.61	25.53	31.87	33.96	31.12
instant ngp(ours)	29.65	25.57	30.30	34.24	31.07

Table 4: The experimental results graph for SLIC segmentation. We conducted experiments testing the results of segmentation based on RGB, rendering error, and our two-stage segmentation method. It can be observed that our method achieves the best performance in terms of both stability and effectiveness.

and the generation of high-quality rendered images. Leveraging the characteristics of superpixels, we devise a novel segmentation, updating, and sampling strategy tailored to them. Our strategy effectively balances the relationship between sampling errors and color information, enabling more efficient information extraction from large-scale inputs. Additionally, we propose a new loss function that better utilizes the characteristics of superpixels. In experimental evaluations, our approach achieves state-of-the-art performance compared to existing methods.

REFERENCES

- [1] Radhakrishna Achanta, Appu Shaji, Kevin Smith, Aurelien Lucchi, Pascal Fua, and Sabine Süsstrunk. 2012. SLIC superpixels compared to state-of-the-art superpixel methods. *IEEE transactions on pattern analysis and machine intelligence* 34, 11 (2012), 2274–2282.
- [2] Daniel Wood Daniel Azuma Wyvern Aldinger, B Curless T Duchamp DH Salesin, and W Stuetzle. 2000. Surface light fields for 3D photography. In *Computer Graphics, SIGGRAPH 2000 Proc.* 287–296.
- [3] Michael Bleyer, Christoph Rhemann, and Carsten Rother. 2011. Patchmatch stereo-stereo matching with slanted support windows.. In *Bmvc*, Vol. 11. 1–11.
- [4] Chris Buehler, Michael Bosse, Leonard McMillan, Steven Gortler, and Michael Cohen. 2001. Unstructured lumigraph rendering. In *Proceedings of the 28th annual conference on Computer graphics and interactive techniques*. 425–432.
- [5] Neill DF Campbell, George Vogiatzis, Carlos Hernández, and Roberto Cipolla. 2008. Using multiple hypotheses to improve depth-maps for multi-view stereo. In *Computer Vision-ECCV 2008: 10th European Conference on Computer Vision, Marseille, France, October 12-18, 2008, Proceedings, Part I* 10. Springer, 766–779.
- [6] Paul E Debevec, Camillo J Taylor, and Jitendra Malik. 2023. Modeling and rendering architecture from photographs: A hybrid geometry-and image-based approach. In *Seminal Graphics Papers: Pushing the Boundaries, Volume 2*. 465–474.
- [7] John Flynn, Michael Broxton, Paul Debevec, Matthew DuVall, Graham Fyffe, Ryan Overbeck, Noah Snavely, and Richard Tucker. 2019. Deepview: View synthesis with learned gradient descent. In *Proceedings of the IEEE/CVF Conference on Computer Vision and Pattern Recognition*. 2367–2376.
- [8] Sara Fridovich-Keil, Alex Yu, Matthew Tancik, Qinhong Chen, Benjamin Recht, and Angjoo Kanazawa. 2022. Plenoxels: Radiance fields without neural networks. In *Proceedings of the IEEE/CVF Conference on Computer Vision and Pattern Recognition*. 5501–5510.
- [9] Yasutaka Furukawa and Jean Ponce. 2009. Accurate, dense, and robust multiview stereopsis. *IEEE transactions on pattern analysis and machine intelligence* 32, 8 (2009), 1362–1376.
- [10] Tao Hu, Shu Liu, Yilun Chen, Tiancheng Shen, and Jiaya Jia. 2022. Efficientnerf efficient neural radiance fields. In *Proceedings of the IEEE/CVF Conference on Computer Vision and Pattern Recognition*. 12902–12911.
- [11] Po-Han Huang, Kevin Matzen, Johannes Kopf, Narendra Ahuja, and Jia-Bin Huang. 2018. Deepmvs: Learning multi-view stereopsis. In *Proceedings of the IEEE Conference on Computer Vision and Pattern Recognition*. 2821–2830.
- [12] Michael Kazhdan, Matthew Bolitho, and Hugues Hoppe. 2006. Proceedings of the fourth Eurographics symposium on Geometry processing.
- [13] Mijeong Kim, Seonguk Seo, and Bohyung Han. 2022. Infonerf: Ray entropy minimization for few-shot neural volume rendering. In *Proceedings of the IEEE/CVF Conference on Computer Vision and Pattern Recognition*. 12912–12921.
- [14] Kiriakos N Kutulakos and Steven M Seitz. 2000. A theory of shape by space carving. *International journal of computer vision* 38 (2000), 199–218.
- [15] Quwei Li, Feichao Li, Jie Guo, and Yanwen Guo. 2023. UHDNeRF: Ultra-High-Definition Neural Radiance Fields. In *Proceedings of the IEEE/CVF International Conference on Computer Vision*. 23097–23108.
- [16] Lingjie Liu, Jiatao Gu, Kyaw Zaw Lin, Tat-Seng Chua, and Christian Theobalt. 2020. Neural sparse voxel fields. *Advances in Neural Information Processing Systems* 33 (2020), 15651–15663.
- [17] Stephen Lombardi, Tomas Simon, Jason Saragih, Gabriel Schwartz, Andreas Lehrmann, and Yaser Sheikh. 2019. Neural volumes: Learning dynamic renderable volumes from images. *arXiv preprint arXiv:1906.07751* (2019).
- [18] Stephen Lombardi, Tomas Simon, Gabriel Schwartz, Michael Zollhoefer, Yaser Sheikh, and Jason Saragih. 2021. Mixture of volumetric primitives for efficient neural rendering. *ACM Transactions on Graphics (ToG)* 40, 4 (2021), 1–13.
- [19] Ben Mildenhall, Pratul P Srinivasan, Rodrigo Ortiz-Cayon, Nima Khademi Kalantari, Ravi Ramamoorthi, Ren Ng, and Abhishek Kar. 2019. Local light field fusion: Practical view synthesis with prescriptive sampling guidelines. *ACM Transactions on Graphics (TOG)* 38, 4 (2019), 1–14.
- [20] Ben Mildenhall, Pratul P Srinivasan, Matthew Tancik, Jonathan T Barron, Ravi Ramamoorthi, and Ren Ng. 2021. Nerf: Representing scenes as neural radiance fields for view synthesis. *Commun. ACM* 65, 1 (2021), 99–106.
- [21] Thomas Müller, Alex Evans, Christoph Schied, and Alexander Keller. 2022. Instant neural graphics primitives with a multiresolution hash encoding. *ACM Transactions on Graphics (ToG)* 41, 4 (2022), 1–15.
- [22] Michael Niemeyer, Lars Mescheder, Michael Oechsle, and Andreas Geiger. 2020. Differentiable volumetric rendering: Learning implicit 3d representations without 3d supervision. In *Proceedings of the IEEE/CVF Conference on Computer Vision and Pattern Recognition*. 3504–3515.
- [23] Michael Niemeyer, Lars M. Mescheder, Michael Oechsle, and Andreas Geiger. 2020. Differentiable Volumetric Rendering: Learning Implicit 3D Representations Without 3D Supervision.. In *CVPR*. 3501–3512.
- [24] Michael Oechsle, Songyou Peng, and Andreas Geiger. 2021. Unisurf: Unifying neural implicit surfaces and radiance fields for multi-view reconstruction. In *Proceedings of the IEEE/CVF International Conference on Computer Vision*. 5589–5599.
- [25] Eric Penner and Li Zhang. 2017. Soft 3d reconstruction for view synthesis. *ACM Transactions on Graphics (TOG)* 36, 6 (2017), 1–11.
- [26] Christian Reiser, Songyou Peng, Yiyi Liao, and Andreas Geiger. 2021. Kilonerf: Speeding up neural radiance fields with thousands of tiny mlps. In *Proceedings of the IEEE/CVF international conference on computer vision*. 14335–14345.
- [27] Lawrence K Saul, Yair Weiss, and Léon Bottou. 2005. *Advances in neural information processing systems 17: proceedings of the 2004 conference*. Vol. 17. MIT Press.
- [28] Johannes L Schonberger and Jan-Michael Frahm. 2016. Structure-from-motion revisited. In *Proceedings of the IEEE conference on computer vision and pattern recognition*. 4104–4113.
- [29] Steven M Seitz and Charles R Dyer. 1999. Photorealistic scene reconstruction by voxel coloring. *International journal of computer vision* 35 (1999), 151–173.
- [30] Vincent Sitzmann, Justus Thies, Felix Heide, Matthias Nießner, Gordon Wetzstein, and Michael Zollhofer. 2019. Deepvoxels: Learning persistent 3d feature embeddings. In *Proceedings of the IEEE/CVF Conference on Computer Vision and Pattern Recognition*. 2437–2446.
- [31] Vincent Sitzmann, Michael Zollhöfer, and Gordon Wetzstein. 2019. Scene representation networks: Continuous 3d-structure-aware neural scene representations. *Advances in Neural Information Processing Systems* 32 (2019).
- [32] Pratul P Srinivasan, Ben Mildenhall, Matthew Tancik, Jonathan T Barron, Richard Tucker, and Noah Snavely. 2020. Lighthouse: Predicting lighting volumes for spatially-coherent illumination. In *Proceedings of the IEEE/CVF Conference on Computer Vision and Pattern Recognition*. 8080–8089.
- [33] Pratul P Srinivasan, Richard Tucker, Jonathan T Barron, Ravi Ramamoorthi, Ren Ng, and Noah Snavely. 2019. Pushing the boundaries of view extrapolation with multiplane images. In *Proceedings of the IEEE/CVF Conference on Computer Vision and Pattern Recognition*. 175–184.
- [34] Cheng Sun, Min Sun, and Hwann-Tzong Chen. 2022. Direct voxel grid optimization: Super-fast convergence for radiance fields reconstruction. In *Proceedings of the IEEE/CVF Conference on Computer Vision and Pattern Recognition*. 5459–5469.
- [35] Shilei Sun, Ming Liu, Zhongyi Fan, Qingliang Jiao, Yuxue Liu, Liquan Dong, and Lingqin Kong. 2024. Efficient ray sampling for radiance fields reconstruction. *Computers & Graphics* 118 (2024), 48–59.
- [36] Richard Szeliski and Polina Golland. 1999. Stereo matching with transparency and matting. *International Journal of Computer Vision* 32, 1 (1999), 45–61.
- [37] Jiaxiang Tang. 2022. Torch-npg: a PyTorch implementation of instant-npg. <https://github.com/ashawkey/torch-npg>.
- [38] Richard Tucker and Noah Snavely. 2020. Single-view view synthesis with multiplane images. In *Proceedings of the IEEE/CVF Conference on Computer Vision and Pattern Recognition*. 551–560.
- [39] Michael Waechter, Nils Moehrle, and Michael Goesele. 2014. Let there be color! Large-scale texturing of 3D reconstructions. In *Computer Vision-ECCV 2014: 13th European Conference, Zurich, Switzerland, September 6-12, 2014, Proceedings, Part V* 13. Springer, 836–850.
- [40] Eric Wahl, Ulrich Hillenbrand, and Gerd Hirzinger. 2003. Surflet-pair-relation histograms: a statistical 3D-shape representation for rapid classification. In *Fourth International Conference on 3-D Digital Imaging and Modeling, 2003. 3DIM 2003. Proceedings*. IEEE, 474–481.
- [41] Peng Wang, Lingjie Liu, Yuan Liu, Christian Theobalt, Taku Komura, and Wenping Wang. 2021. NeuS: Learning Neural Implicit Surfaces by Volume Rendering for Multi-view Reconstruction. *Advances in Neural Information Processing Systems* 34 (2021), 27171–27183.
- [42] Yiming Wang, Qin Han, Marc Habermann, Kostas Daniilidis, Christian Theobalt, and Lingjie Liu. 2023. NeuS2: Fast learning of neural implicit surfaces for multi-view reconstruction. In *Proceedings of the IEEE/CVF International Conference on Computer Vision*. 3295–3306.
- [43] Zhou Wang, Alan C Bovik, Hamid R Sheikh, and Eero P Simoncelli. 2004. Image quality assessment: from error visibility to structural similarity. *IEEE transactions on image processing* 13, 4 (2004), 600–612.
- [44] Zhongshu Wang, Lingzhi Li, Zhen Shen, Li Shen, and Liefeng Bo. 2022. 4k-nerf: High fidelity neural radiance fields at ultra high resolutions. *arXiv preprint arXiv:2212.04701* (2022).
- [45] Jiawei Yang, Marco Pavone, and Yue Wang. 2023. FreeNeRF: Improving Few-shot Neural Rendering with Free Frequency Regularization. In *Proceedings of the IEEE/CVF Conference on Computer Vision and Pattern Recognition*. 8254–8263.
- [46] Lior Yariv, Yoni Kasten, Dror Moran, Meirav Galun, Matan Atzmon, Basri Ronen, and Yaron Lipman. 2020. Multiview neural surface reconstruction by disentangling geometry and appearance. *Advances in Neural Information Processing Systems* 33 (2020), 2492–2502.
- [47] Lior Yariv, Yoni Kasten, Dror Moran, Meirav Galun, Matan Atzmon, Basri Ronen, and Yaron Lipman. 2020. Multiview neural surface reconstruction by disentangling geometry and appearance. *Advances in Neural Information Processing Systems* 33 (2020), 2492–2502.
- [48] Lior Yariv, Yoni Kasten, Dror Moran, Meirav Galun, Matan Atzmon, Basri Ronen, and Yaron Lipman. 2020. Multiview neural surface reconstruction by disentangling geometry and appearance. *Advances in Neural Information Processing Systems* 33 (2020), 2492–2502.

- 1045 [49] Richard Zhang, Phillip Isola, Alexei A Efros, Eli Shechtman, and Oliver Wang.
1046 2018. The unreasonable effectiveness of deep features as a perceptual metric.
1047 In *Proceedings of the IEEE conference on computer vision and pattern recognition*.
1048 586–595.
- 1049 [50] Wenyuan Zhang, Ruofan Xing, Yunfan Zeng, Yu-Shen Liu, Kanle Shi, and
1050 Zhizhong Han. 2023. Fast learning radiance fields by shooting much fewer
1051 rays. *IEEE Transactions on Image Processing* (2023).
- 1052 [51] Tinghui Zhou, Richard Tucker, John Flynn, Graham Fyffe, and Noah Snavely.
1053 2018. Stereo magnification: Learning view synthesis using multiplane images.
1054 *arXiv preprint arXiv:1805.09817* (2018).
- 1055 1103
- 1056 1104
- 1057 1105
- 1058 1106
- 1059 1107
- 1060 1108
- 1061 1109
- 1062 1110
- 1063 1111
- 1064 1112
- 1065 1113
- 1066 1114
- 1067 1115
- 1068 1116
- 1069 1117
- 1070 1118
- 1071 1119
- 1072 1120
- 1073 1121
- 1074 1122
- 1075 1123
- 1076 1124
- 1077 1125
- 1078 1126
- 1079 1127
- 1080 1128
- 1081 1129
- 1082 1130
- 1083 1131
- 1084 1132
- 1085 1133
- 1086 1134
- 1087 1135
- 1088 1136
- 1089 1137
- 1090 1138
- 1091 1139
- 1092 1140
- 1093 1141
- 1094 1142
- 1095 1143
- 1096 1144
- 1097 1145
- 1098 1146
- 1099 1147
- 1100 1148
- 1101 1149
- 1102 1150